Error Suppression of Magnetic Encoder Using Improved Second-order Generalized Integrator and Harmonic Decoupling Network

Shuang Wang, Hanyi He, Tianren Li, Hao Li and Jianfei Zhao[*]
(School of Mechatronic Engineering and Automation, Shanghai University, Shanghai 200444, China)

Abstract: Compared with traditional position sensors, magnetic encoders do not require optical components, which are easily damaged, have complex winding structures, and have higher reliability, better environmental resistance, and stronger vibration resistance. However, owing to some non-ideal factors, the output angle of the magnetic encoder may have an amplitude error, phase offset, DC bias, and harmonic deviation, which greatly affect the decoding accuracy. A magnetic encoder error compensation algorithm is proposed based on an improved second-order generalized integrator (ISOGI). First, the errors existing in the magnetic encoder are analyzed and verified and then a dual improved second-order generalized integrator harmonic decoupling network phase-lock loop (DISOGI-HDN-PLL) is proposed, which has the ability to compensate for low-order harmonics and other errors. This proposed method compensates for various errors under constant and high-speed conditions. In addition, it has good response and robustness, effectively improving the decoding accuracy of the magnetic encoder. Simulation and experimental results demonstrate the effectiveness and applicability of the proposed algorithm.

Keywords: Error compensation, magnetic encoder, phase-locked loop (PLL), second-order generalized integrator (SOGI)

1 Introduction

Magnetic encoders are widely used as rotor-position detection devices in servomotors, handheld gimbals, precision machine tool processing, underwater robots, and aerospace [1-2]. Magnetic encoders are favored for their high-frequency characteristics, rapid response times, noncontact sensing capabilities, and suitability for challenging conditions such as oil, dust, and wide temperature variations compared with photoelectric encoders [3-5]. Furthermore, their simple structure, resilience to significant impacts, and ease of miniaturization make them suitable for applications in systems with high requirements for reliability and stability [6].

The magnetic encoder outputs sine and cosine signals that contain angle information [7-8]. By decoding these signals, physical quantities such as the rotational angle can be converted into electrical signals. However, magnetic encoders are susceptible to limitations imposed by manufacturing techniques and installation processes, which result in nonideal errors in their output [9], including harmonic distortion [10], amplitude deviation [11], phase shift [12], and DC offset [13]. These errors reduce the accuracy of magnetic encoders [14].

Several compensation methods have been proposed to improve the angle accuracy. The second-order generalized integrator (SOGI) does not exhibit amplitude deviation or phase offset at the center frequency point [15] and can extract the positive sequence of the sine and cosine, suppressing the amplitude and phase errors, which is worth further investigation. An extended SOGI application for stator-flux estimation in sensor-less AC motor drives has been proposed [16]; however, this algorithm cannot achieve high-precision suppression of the DC offset. A frequency-fixed SOGI-based PLL (FFSOGI-PLL) has been proposed to ensure stability and simple implementation [17]; however, this method generates additional harmonics, the suppression of which requires higher costs. A novel discrete-time nonadaptive SOGI-FLL based on the gradient descent

Manuscript received May 30, 2024; revised August 5, 2024; accepted September 11, 2024. Date of publication March 31, 2026; date of current version May 30, 2025.
* Corresponding Author, E-mail: jfzhao@shu.edu.cn
Digital Object Identifier:10.23919/CJEE.2025.000150

algorithm has been proposed [18]; however, its complex structure leads to excessive resource consumption. Therefore, the current study aims to use SOGI to eliminate all non-ideal errors in magnetic encoders.

Other studies have proposed various algorithms for error suppression. The dual synchronous rotating coordinate phase-locked loop algorithm can extract the positive sequence of unbalanced sine and cosine signals with high accuracy; however, it requires decomposing the signal into a dual rotating coordinate system, and the subsequent forward and backward decoupling network is complex, which affects the closed-loop transient response speed [19]. Kalman filtering and curve fitting methods have been extended to compensate for errors, which can improve output accuracy; however, these algorithms can also lead to an increase in transmission delay [20]. A code compensator based on optimization theories has been applied to correct the non-ideal signals of the output [21]. Two small-signal equivalent modified quasi-type-1 PLLs (QT1-PLL) with frequency and phase forward compensation terms were used to eliminate the frequency ramp-induced phase error, achieving zero steady-state error and lower peak overshoot; however, they do not address the measured offset and harmonic rejection [22]. A calibration method based on an adaptive linear neural network (ADALINE) has been proposed to reduce the effect of non-idealities [23]. Although the above literature has made significant contributions to improving accuracy, all approaches lack effective suppression of harmonic errors, which reduces the decoding accuracy and tracking speed of the magnetic encoder.

There are many solutions for harmonic suppression, as follows. A two-layer radial basis correction method has been proposed [24], in which the first layer is used for the adaptive correction of defects in the encoder signal, while the second layer serves as an inference engine that maps orthogonal encoder signals to higher-order sine signals. This method offers advantages over the lookup table approach [25] in terms of storage memory and execution speed; however, this method is often limited by the manufacturing process of magnetic encoders. A sensorless control scheme based on a sliding-mode observer with an orthogonal PLL incorporating two synchronous frequency-extract filters (SFFs) has been proposed [26], which can filter out high-order harmonics simultaneously regardless of whether the harmonics are sourced from the air-gap magnetic field or the nonlinearity of the inverter; however, it only has a suppressive effect on the fifth and seventh harmonics. By using an oscilloscope to capture the output voltage waveforms of Hall sensors in real time, the corresponding conversion errors can be calculated based on the relevant error expressions, and the total error can then be stored in a ROM table. Online compensation can be performed by referencing the lookup table [11]. A novel encoder structure and signal-processing method based on a lookup table were proposed, in which a higher-resolution optical encoder was used for calibration and three signals were used in different regions of the lookup table [27]; however, this was limited by accuracy. Most studies have not addressed the suppression of low-order harmonics.

This study proposes an effective decoding algorithm, namely, the dual improved second-order generalized integrator harmonic decoupling network phase-lock loop (DISOGI-HDN-PLL), to compensate for errors in the magnetic encoder. The main contributions of this study are as follows. First, a dual second-order generalized integrator (DSOGI) was proposed to extract the positive sequences of sine and cosine signals to compensate for amplitude and phase errors. In addition, a DISOGI based on the DSOGI was proposed, which not only suppresses phase and amplitude errors of the SOGI but also suppresses DC offset errors. Finally, a harmonic decoupling network (HDN) was proposed to extract the fundamental frequency signal and various harmonics, and a second-order frequency-locked loop (FLL) was designed to provide real-time feedback of the estimated frequency of the system to the SOGI to achieve frequency adaptation, effectively suppressing low-order harmonic errors.

The remainder of this paper is organized as follows. Section 2 introduces the principles and decoding algorithm of the magnetic encoder, followed by an analysis of the errors and verification through simulation. Section 3 presents a detailed introduction to the proposed algorithm. Section 4 verifies the reliability and stability of the proposed algorithm, and

Section 5 concludes the paper.

2 Error analysis of magnetic encoder

The structure of the magnetic encoder is shown in Fig. 1. The magnetic grid is installed coaxially with the motor rotor, which rotates to generate a rotating magnetic field, and the magnetoresistive element detects the change in the magnetic field and generates sine and cosine signals containing the rotor position [28-29], which can be expressed as

$$\begin{cases} U_{\sin} = U_m \sin\theta_m \\ U_{\cos} = U_m \cos\theta_m \end{cases} \tag{1}$$

where U_m is the amplitude and θ_m is the electrical angle.

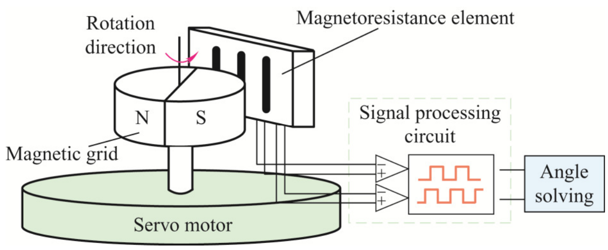

Fig. 1 Structure of the magnetic encoder

2.1 Decoding algorithm based on PLL

Currently, the most widely used algorithm in the industry is the PLL, which can effectively calculate the angle of the rotor [30-32]. As a closed-loop system, a PLL usually consists of a phase detector (PD), loop filter (LF), and voltage-controlled oscillator (VCO). The sine and cosine signals of the magnetic encoder were used as input signals for the PLL, as shown in Fig. 2.

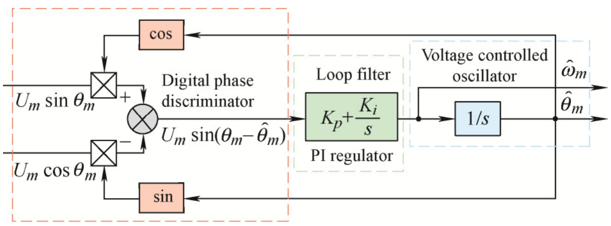

Fig. 2 Phase-locked loop

By comparing the voltage phase signal input to the PLL with the voltage phase signal output of the loop through a phase detector, the phase difference is converted into the corresponding voltage signal and then processed by a loop filter to suppress noise and high-frequency signals. Finally, the output information of the loop filter is fed into a VCO. When the input signal frequencies of the phase detector and loop filter are consistent, the phase difference between them remains constant, ensuring that the frequency of the VCO does not change, achieving phase locking.

In Fig. 2, U_m is the amplitude of the input signal; $\hat{\theta}_m$ is the estimated angle; $\hat{\omega}$ is the angular velocity; $\hat{\omega}_m$ is the estimated angular velocity; K_p and K_i are the proportional and integral coefficients, respectively.

The error signal U_{err} output by the digital phase discriminator can be expressed as

$$U_{err} = U_m \sin(\theta_m - \hat{\theta}_m) \tag{2}$$

The angle tracking error $\Delta\theta$ is given by

$$\Delta\theta = \theta_m - \hat{\theta}_m \tag{3}$$

When the error $\Delta\theta$ is small, U_{err} is given by

$$U_{err} = U_m \sin(\theta_m - \hat{\theta}_m) \approx U_m(\theta_m - \hat{\theta}_m) \tag{4}$$

$\Delta\theta$ can be obtained after the PI regulator, and $\hat{\theta}_m$ can be obtained by integrating the estimated speed. After closed-loop feedback, U_{err} approaches 0, which corresponds to $\hat{\theta}_m = \theta_m$, indicating that the system is stable.

2.2 Error analysis

Owing to the number of magnetic poles and tracks and the installation bias of the magnetic-sensitive components [33-34], the magnetic encoder's output exhibits the following errors.

2.2.1 Amplitude deviation

The two-phase sine and cosine signals with amplitude deviation outputs from magnetic encoding are given by

$$\begin{cases} U_{\sin} = \alpha U_m \sin\theta_m \\ U_{\cos} = U_m \cos\theta_m \end{cases} \tag{5}$$

where U_m is the amplitude of the sine and cosine signals of the magnetic encoder, θ_m is the electrical angle, and α is the amplitude error coefficient.

The U_{err} output from the digital PD of the PLL is given by

$$U_{err} = U_m[\sin(\theta_m - \hat{\theta}_m)] + (\alpha-1)U_m \sin\theta_m \cos\hat{\theta}_m \tag{6}$$

When U_{err}=0, the PLL stopped tracking the input angle. In practical situations, the angle tracking error $\Delta\theta_m$ is relatively small and can be approximated as

$\sin(\Delta\theta_m)\approx\Delta\theta_m$, $\theta_m\approx\hat{\theta}_m$. $\Delta\theta_m$ can be obtained as follows

$$\Delta\theta_m=-\frac{(\alpha-1)}{2}\sin(2\theta_m) \tag{7}$$

Simulation models based on Simulink were constructed to verify the impact of different errors. Given an amplitude deviation α=0.8, input signal frequency f=50 Hz, input amplitude U_m=1 V, the angle calculated by the PLL and the corresponding angle error are shown in Fig. 3.

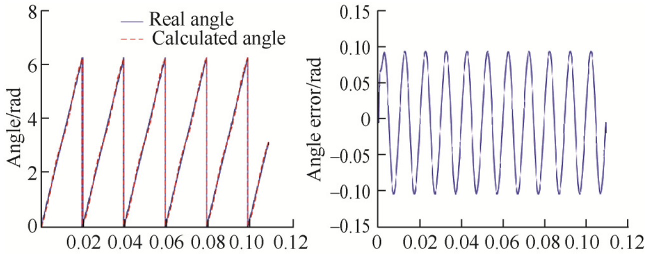

(a) Angle (b) Angle error

Fig. 3 Simulation results with amplitude errors

It can be seen that $\Delta\theta_m$ exhibits a second harmonic characteristic, and is proportional to the amplitude error coefficient. The magnitude of the error is 0.1 rad, the frequency is twice that of the input, and the error waveform takes the form of a sinusoidal wave, verifying Eq. (7).

2.2.2 Phase shift

When the output of the magnetic encoder contains a phase shift

$$\begin{cases}U_{\sin}=U_m\sin(\theta_m+\varphi)\\U_{\cos}=U_m\cos\theta_m\end{cases} \tag{8}$$

where φ is the phase shift coefficient.

The angle tracking error $\Delta\theta_m$ is given by

$$\Delta\theta_m=-\frac{\varphi}{2}(1+\cos 2\theta_m) \tag{9}$$

While maintaining the input frequency and amplitude constant, a phase error of φ = π/18 was introduced into the sinusoidal signal to verify its impact, as shown in Fig. 4.

It can be seen that $\Delta\theta_m$ has a cosine relationship with twice the angle θ_m, and is proportional to the phase error φ. The magnitude of the error is 0.092 rad, with a frequency twice that of the input. This is consistent with the theoretical results of Eq. (9).

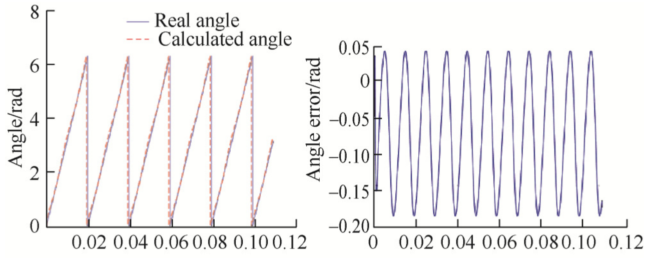

(a) Angle (b) Angle error

Fig. 4 Simulation results with phase errors

2.2.3 DC offset

The output of the magnetic encoder with a DC offset is

$$\begin{cases}U_{\sin}=U_m\sin\theta_m+U_{dc}\\U_{\cos}=U_m\cos\theta_m\end{cases} \tag{10}$$

where U_{dc} is the DC offset coefficient.

$\Delta\theta_m$ can be obtained as

$$\Delta\theta_m=-\frac{U_{dc}}{U_m}\cos\theta_m \tag{11}$$

Given the DC offset of the sinusoidal signal U_{dc} = 0.2 V, the simulation results are shown in Fig. 5. It can be seen that $\Delta\theta_m$ has a cosine relationship with θ_m and is proportional to U_{dc}. The magnitude of the error is 0.201 rad, the error waveform is a cosine wave, and its frequency is the same as that of the input frequency, which verifies Eq. (11).

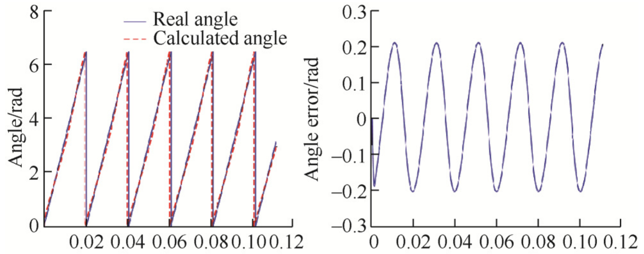

(a) Angle (b) Angle error

Fig. 5 Simulation results with DC offset errors

2.2.4 Harmonic distortion

When the output of the magnetic encoder contains only harmonic distortions

$$\begin{cases}U_{\sin}=U_m\sin\theta_m+\sum_{n=2}^{k}U_n\sin(n\theta_m)\\U_{\cos}=U_m\cos\theta_m+\sum_{n=2}^{k}U_n\cos(n\theta_m)\end{cases} \tag{12}$$

where k is the number of harmonics; n is the harmonic order; and U_n is the amplitude of the nth harmonic.

Similarly, $\Delta\theta_m$ at this time is given by

$$\Delta\theta_m = -\frac{U_n}{U_m}\sum_{n=2}^{k}\sin[(n-1)\theta_m] \tag{13}$$

As shown in Fig. 6, the third-harmonic distortion U_3= 0.1 V was introduced for verification.

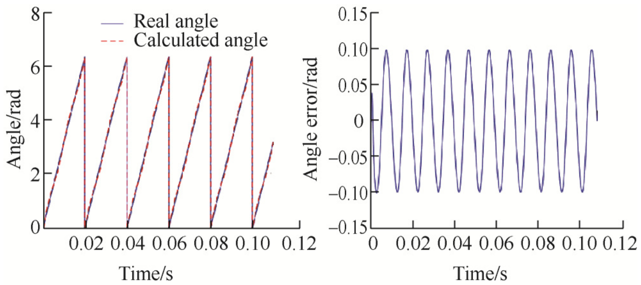

(a) Angle (b) Angle error

Fig. 6 Simulation results with harmonic errors

It can be seen that the magnitude of the error is 0.1 rad, and the frequency of the error is twice the fundamental frequency of the input, which is consistent with Eq. (13). When the output of the magnetic encoder contains harmonic distortion, the nth harmonic generates a (n–1)th harmonic component in $\Delta\theta_m$, and $\Delta\theta_m$ is proportional to the harmonic amplitude .

3 Error compensation algorithm

3.1 Double Second-order generalized integrator

The structure of a traditional SOGI is illustrated in Fig. 7, where v is the input, ε denotes the error, k is the damping factor, and $\hat{\omega}_m$ is the center frequency.

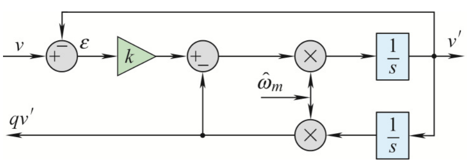

Fig. 7 Block diagram of the traditional SOGI structure

When $\hat{\omega}_m = \omega_m$, the outputs v' and qv' have the same amplitude, but the phase of qv' lags 90° behind v'; q is the orthogonal factor, and v' has the same amplitude and phase as v. The SOGI's transfer function can be expressed as

$$\begin{cases} G_1(s) = \dfrac{v'(s)}{v(s)} = \dfrac{k\hat{\omega}_m s}{s^2 + k\hat{\omega}_m s + \hat{\omega}_m^2} \\ G_2(s) = \dfrac{qv'(s)}{v(s)} = \dfrac{k\hat{\omega}_m^2}{s^2 + k\hat{\omega}_m s + \hat{\omega}_m^2} \end{cases} \tag{14}$$

where $v'(s)$ is the output of the SOGI, and q is the orthogonality factor.

From the Bode diagram in Fig. 8, it can be seen that $G_1(s)$ is a second-order bandpass filter whose bandwidth is related to k; $G_2(s)$ is a second-order low-pass filter. The smaller the k value, the better the filtering, but the longer the transient response time.

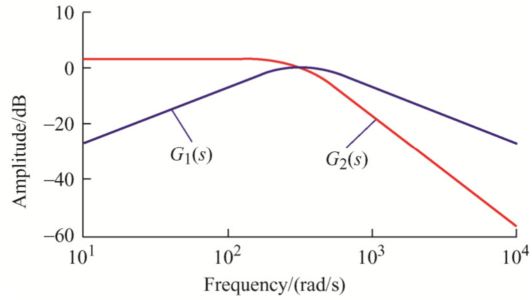

Fig. 8 Bode diagrams of $G_1(s)$ and $G_2(s)$

The DSOGI employs two SOGIs to extract the positive sequences of the sine and cosine outputs of the magnetic encoder, thereby compensating for amplitude and phase errors, as shown in Fig. 9. In Fig. 9, v_α and v_β are the outputs of the magnetic encoder; v'_α, qv'_α, v'_β, and qv'_β are the orthogonal signals generated by the SOGI; and $v_\alpha^{+'}$ and $v_\beta^{+'}$ are the positive sequences.

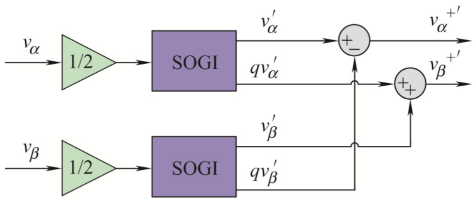

Fig. 9 Block diagram of DSOGI structure

If the output of the magnetic encoder contains amplitude deviation and phase shift, it can be expressed as follows

$$\begin{cases} U_{\cos} = \cos(\theta_m) \\ U_{\sin} = \alpha\sin(\theta_m + \varphi) \end{cases} \tag{15}$$

where α is the amplitude error and φ is the phase error.

From Eq. (14), the transfer functions $X(s)$ and $Y(s)$ are

$$X(s) = \frac{v_\alpha^{+'}(s)}{v_\alpha(s)} = \frac{k\hat{\omega}_m}{2}\cdot\left[\frac{s^2 - \alpha\hat{\omega}_m(\omega_m\cos\varphi + s\sin\varphi)}{s(s^2 + k\hat{\omega}_m s + \hat{\omega}_m^2)}\right] \tag{16}$$

$$Y(s) = \frac{v_\beta^{+'}(s)}{v_\beta(s)} = \frac{k\hat{\omega}_m}{2}\cdot\left[\frac{\hat{\omega}_m s + \alpha s(\omega_m\cos\varphi + s\sin\varphi)}{\alpha(\omega_m\cos\varphi + s\sin\varphi)(s^2 + k\hat{\omega}_m s + \hat{\omega}_m^2)}\right] \tag{17}$$

where $v_\alpha(s)$ and $v_\beta(s)$ are the outputs of the magnetic encoder, and $v_\alpha^{+'}(s)$ and $v_\beta^{+'}(s)$ are the positive sequences.

The amplitudes and phases of $X(s)$ and $Y(s)$ are given by

$$\begin{cases} |X| = \dfrac{k\hat{\omega}_m}{2}\sqrt{a^2+b^2} \\ \arg(X) = \arctan\dfrac{b}{a} \\ |Y| = \dfrac{k\hat{\omega}_m\sqrt{e^2+f^2}}{2\alpha(c^2+d^2)} \\ \arg(Y) = \arctan\dfrac{f}{e} \end{cases} \tag{18}$$

where

$$\begin{cases} a = \alpha\hat{\omega}_m(\omega_m^2-\hat{\omega}_m^2)\sin\varphi + k\omega_m\hat{\omega}_m(\omega_m+\alpha\hat{\omega}_m\cos\varphi) \\ b = \alpha k\omega_m\hat{\omega}_m^2\sin\varphi - (\omega_m^2-\hat{\omega}_m^2)(\omega_m+\alpha\hat{\omega}_m\cos\varphi) \\ c = (\hat{\omega}_m^2-\omega_m^2)\cos\varphi - k\omega_m\hat{\omega}_m\sin\varphi \\ d = k\omega_m\hat{\omega}_m\cos\varphi + (\hat{\omega}_m^2-\omega_m^2)\sin\varphi \\ e = \alpha\omega_m(b\cos\varphi - a\sin\varphi) + b\hat{\omega}_m \\ f = \alpha\omega_m(a\cos\varphi + b\sin\varphi) + a\hat{\omega}_m \end{cases}$$

When $\hat{\omega}_m = \omega_m$, from Eqs. (16)-(18), combined with the Fourier transform, the output of the DSOGI can be simplified as Eq. (19).

$$\begin{cases} v_\alpha^{+'}(t) = \dfrac{\sqrt{1+\alpha^2+2\alpha\cos\varphi}}{2}\cos(\omega_m t+\tau) \\ v_\beta^{+'}(t) = \dfrac{\sqrt{1+\alpha^2+2\alpha\cos\varphi}}{2}\sin(\omega_m t+\gamma) \end{cases} \tag{19}$$

τ and γ can be expressed as

$$\begin{cases} \tau = \arctan\dfrac{\alpha\sin\varphi}{1+\alpha\cos\varphi} \\ \gamma = \varphi - \arctan\dfrac{\sin\varphi}{\alpha+\cos\varphi} \end{cases} \tag{20}$$

In Eq. (20), it is easy to prove that $\tau = \gamma$ by using the trigonometric function. Therefore, the DSOGI can effectively eliminate amplitude and phase errors. Then, the PLL is used to calculate the positive sequence of the DSOGI, which can measure the high-precision angle.

3.2 Improved second-order generalized integrator

Combining the low-pass filtering characteristics of $G_2(s)$ in Eq. (14), the output qv' becomes distorted because of the DC offset of the magnetic encoder. Therefore, the improved second-order generalized integrator (ISOGI) was proposed to suppress the DC offset, as shown in Fig. 10. The transfer function is expressed by Eq. (21).

$$\begin{cases} G_3(s) = \dfrac{v_m'(s)}{v(s)} = \dfrac{k\hat{\omega}_m s}{s^2+k\hat{\omega}_m s+\hat{\omega}_m{}^2} \\ G_4(s) = \dfrac{qv_m'(s)}{v(s)} = \dfrac{k\hat{\omega}_m s(\hat{\omega}_m - s)}{(s+\hat{\omega}_m)(s^2+k\hat{\omega}_m s+\hat{\omega}_m{}^2)} \end{cases} \tag{21}$$

where $v(s)$ is the ISOGI input, and $v_m'(s)$ is the ISOGI output.

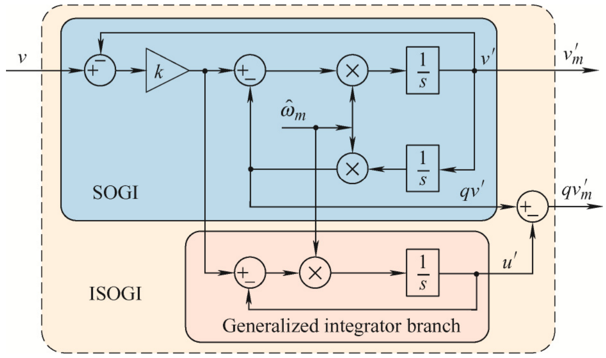

Fig. 10 Simulation results with harmonic errors

In Eq. (21), $G_4(s)$ changes compared with $G_2(s)$, whose Bode diagram is shown in Fig. 11. $G_4(s)$ has bandpass-filtering characteristics that can effectively filter the DC offset.

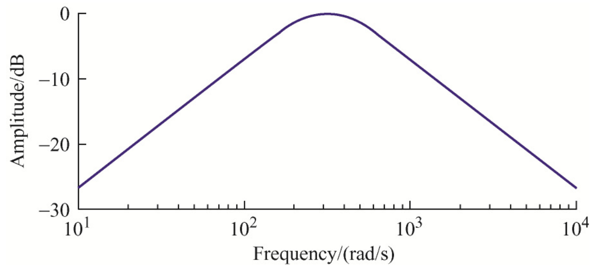

Fig. 11 Bode diagram of $G_4(s)$

Fig. 12 shows the structure of the DISOGI-PLL, in which two ISOGIs are used as substitutes for the SOGIs. The angular velocity ω_m generated by the PLL is fed back to the ISOGIs to form a closed-loop system.

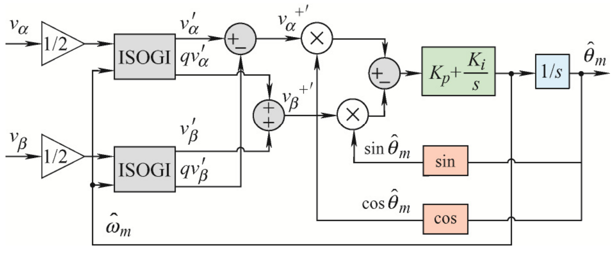

Fig. 12 Structure of the DISOGI-PLL

3.3 Harmonic suppression algorithm

3.3.1 Second-order frequency locked loops

A general FLL cannot accurately track the motor angular frequency during constant-acceleration operation [30]. To ensure the stability of the motor during constant acceleration and to consider the characteristics of the magnetic encoder's sine and cosine output, a second-order FLL was designed, as shown in Fig. 13.

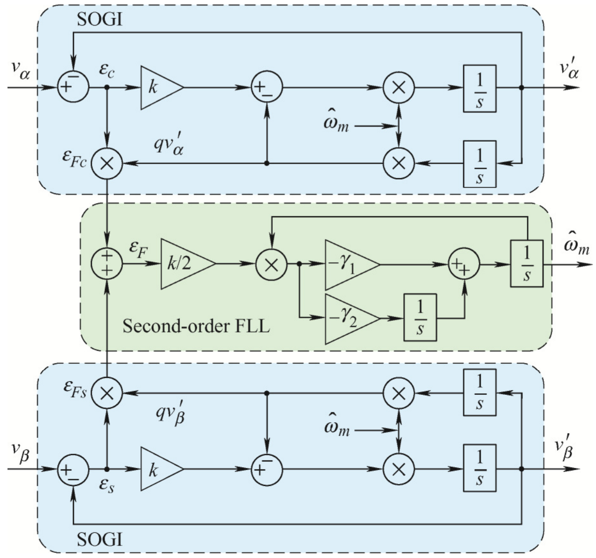

Fig. 13 Structure of the second-order FLL

As shown in Fig. 13, because the two-phase inputs v_α and v_β are symmetric, v_α is considered an example for the analysis. The state variable of the SOGI is defined as

$$\begin{cases} x_1 = v'_\alpha \\ x_2 = qv'_\alpha \end{cases} \tag{22}$$

where v'_α is the output and q is the orthogonality factor.

The state-space equation of the SOGI is

$$\begin{bmatrix} \dot{x}_1 \\ \dot{x}_2 \end{bmatrix} = \begin{bmatrix} -k\hat{\omega}_m & -\hat{\omega}_m \\ \hat{\omega}_m & 0 \end{bmatrix} \begin{bmatrix} x_1 \\ x_2 \end{bmatrix} + \begin{bmatrix} k\hat{\omega}_m \\ 0 \end{bmatrix} v_\alpha \tag{23}$$

$$\begin{bmatrix} v'_\alpha \\ qv'_\alpha \end{bmatrix} = \begin{bmatrix} 1 & 0 \\ 0 & 1 \end{bmatrix} \begin{bmatrix} x_1 \\ x_2 \end{bmatrix} \tag{24}$$

where k is the damping factor, and $\hat{\omega}_m$ is the central frequency. The estimated error ε_c from Eq. (23) is

$$\varepsilon_c = v_\alpha - v'_\alpha = (\dot{x}_1 + \hat{\omega}_m x_2) / k\hat{\omega}_m \tag{25}$$

when the cosine-channel $v_\alpha = \cos(\omega_m t)$. According to the characteristic curves of $G_1(s)$, Eq. (26) can be obtained as follows

$$qv'_\alpha = -\frac{\hat{\omega}_m}{\omega_m} \left| G_1(j\omega_m) \right| \sin[\omega_m t + \angle G_1(j\omega_m)] \tag{26}$$

Based on qv'_α and v_α, the error equation is

$$\varepsilon_c = \frac{\hat{\omega}_m^2 - \omega_m^2}{k\hat{\omega}_m^2} x_2 \tag{27}$$

ε_{Fc} of the output of the cosine channel from SOGI to FLL can be expressed as

$$\varepsilon_{Fc} = \varepsilon_c x_2 = -\frac{\hat{\omega}_m^2 - \omega_m^2}{k\hat{\omega}_m^2} x_2^2 \tag{28}$$

From Eq. (26) and near the operating point, the existing conditions are $|G_1(j\omega_m)| \to 1$, $\angle G_1(j\omega_m) \to 0$, and $\hat{\omega}_m \to \omega_m$. Therefore, x_2^2 can be approximated as

$$x_2^2 = \sin^2(\omega_m t) \tag{29}$$

We define the angular frequency tracking error of the FLL as $\tilde{\omega}_m = \omega_m - \hat{\omega}_m$. Substituting Eq. (29) into Eq. (28) yields the following

$$\varepsilon_{Fc} = -\frac{2\tilde{\omega}_m}{k\hat{\omega}_m} \sin^2(\omega_m t) \tag{30}$$

Similarly, when $v_\beta = \sin(\omega_m t)$

$$\varepsilon_{Fs} = -\frac{2\tilde{\omega}_m}{k\hat{\omega}_m} \cos^2(\omega_m t) \tag{31}$$

The sum of ε_{Fc} and ε_{Fs} can be expressed as

$$\varepsilon_F = \varepsilon_{Fc} + \varepsilon_{Fs} = -\frac{2\tilde{\omega}_m}{k\hat{\omega}_m} \tag{32}$$

where the product of the error signal ε_c and the output signal qv'_α is ε_{Fc}, and the product of ε_s and qv'_β is ε_{Fs}.

It can be seen from Eq. (32) that ε_F contains the estimated angular frequency $\hat{\omega}_m$ and its error $\tilde{\omega}_m$. In addition, the overlay of the two signals eliminates sinusoidal fluctuations and improves the angular frequency accuracy. However, it is necessary to improve the tracking accuracy of the FLL under constant acceleration conditions.

The second-order FLL is designed according to ε_F.

$$\begin{cases} \dot{\hat{\omega}}_m = \hat{\alpha} - \gamma_1 k\hat{\omega}_m \varepsilon_F / 2 \\ \dot{\hat{\alpha}} = -\gamma_2 k\hat{\omega}_m \varepsilon_F / 2 \end{cases} \tag{33}$$

where γ_1, γ_2 are the gain, $\hat{\alpha}$ is the estimated angle acceleration, and $\dot{\hat{\omega}}_m$ and $\dot{\hat{\alpha}}$ are the derivatives of $\hat{\omega}_m$ and $\hat{\alpha}$.

To analyze the convergence, we substitute Eq. (32) into Eq. (33)

$$\begin{cases} \dot{\hat{\omega}}_m = \hat{\alpha} + \gamma_1 \tilde{\omega}_m \\ \dot{\hat{\alpha}} = \gamma_2 \tilde{\omega}_m \end{cases} \tag{34}$$

where α is the angular acceleration, and $\dot{\alpha} = \delta(t)$ and $\delta(t)$ are bounded quantities. Let the angle acceleration estimation error $\tilde{\alpha} = \alpha - \hat{\alpha}$. Based on the known $\dot{\omega}_m = \alpha$, the error dynamics in Eq. (35) can be deduced from Eq. (34) as

$$\begin{cases} \dot{\tilde{\omega}}_m = \tilde{\alpha} - \gamma_1 \tilde{\omega}_m \\ \dot{\tilde{\alpha}} = \delta(t) - \gamma_2 \tilde{\omega}_m \end{cases} \tag{35}$$

Then, Eq. (36) is obtained from Eq. (35).

$$\ddot{\tilde{\omega}}_m + \gamma_1 \dot{\tilde{\omega}}_m + \gamma_2 \tilde{\omega}_m = \delta(t) \tag{36}$$

This was obtained using the final value theorem, as shown in Eq. (37)

$$\lim_{t\to\infty} \tilde{\omega}_m(t) = \lim_{s\to 0} \frac{s\delta(s)}{s^2 + \gamma_1 s + \gamma_2} \tag{37}$$

$\tilde{\omega}_m$ eventually converges to 0; therefore, the second-order FLL was stable. When the input changes at a constant velocity or acceleration, the angular frequency estimation error $\tilde{\omega}_m$ converges to 0. Therefore, when the motor operates in the aforementioned modes, the second-order FLL can realize an unsteady error when estimating the frequency.

3.3.2 Harmonic decoupling network (HDN)

The ISOGI transfer function has bandpass filtering characteristics that can suppress higher-order harmonics. However, it cannot efficiently suppress the lower harmonics with high response characteristics.

Therefore, the HDN algorithm is proposed, as shown in Fig. 14, in which the separated harmonic is sent to the original signal, and the specified subharmonics are weakened at the signal source to improve the decoding accuracy.

The HDN can be adjusted to different frequencies, and the fundamental frequencies of the output sine and cosine can be accurately extracted. As long as the center frequency $\hat{\omega}_m$ of SOGI is equal to the input frequency ω_m, HDN can eliminate multiple specified subharmonic errors.

To suppress the second and third harmonics, each phase of the HDN contains three SOGIs for extracting the above harmonics. The second-order FLL delivers the estimated angular frequency $\hat{\omega}_m$ to the SOGI in real time. The FLL output frequency $\hat{\omega}_m$ is multiplied by the specified sub-coefficient n, which is called the specified subharmonic frequency, and sent to the SOGI.

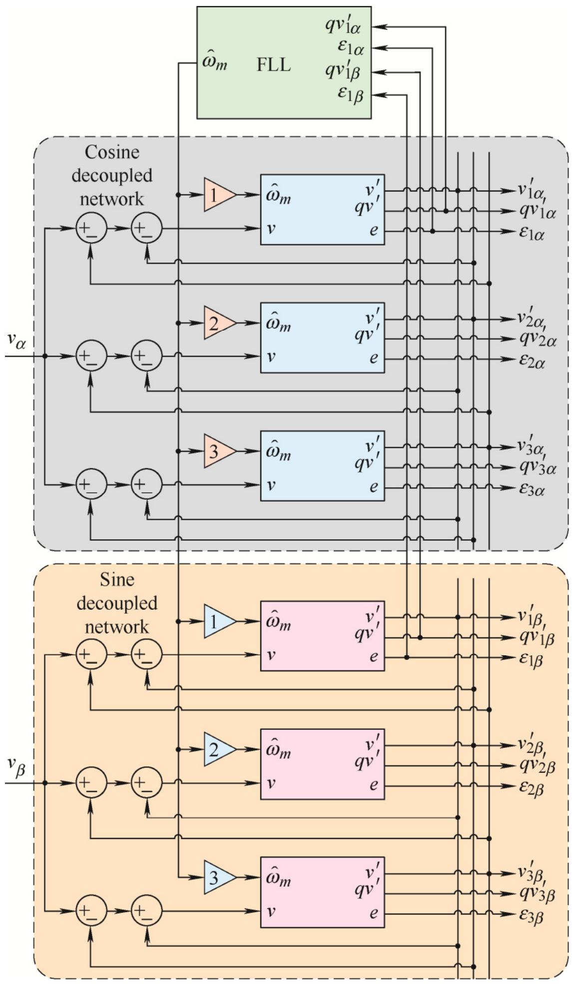

Fig. 14 Structure of the HDN

The relationship between the input and output is expressed by Eq. (38).

$$\begin{cases} v'_{1m} = D_1(s)(v_m - v'_{2m} - v'_{3m}) \\ v'_{2m} = D_2(s)(v_m - v'_{1m} - v'_{3m}) \\ v'_{3m} = D_3(s)(v_m - v'_{1m} - v'_{2m}) \end{cases} \tag{38}$$

where m represents the α or β axis. $D_1(s)$, $D_2(s)$, and $D_3(s)$ are given in Eq. (39), where n = 1, 2, 3.

$$D_n(s) = \frac{v'(s)}{v(s)} = \frac{k(n\hat{\omega}_m)s}{s^2 + k(n\hat{\omega}_m)s + (n\hat{\omega}_m)^2} \tag{39}$$

The transfer function of $v'_{1\alpha}/v_\alpha$ and $v'_{1\beta}/v_\beta$ is

$$F(s) = D_1 \frac{1 - D_2 - D_3 + D_2 D_3}{1 - D_2 D_3 - D_1 D_2 - D_1 D_3 + 2 D_1 D_2 D_3} \tag{40}$$

Taking the motor angular frequency $\omega_m = 100\pi$ rad as an example, k is set to $\sqrt{2}$, and the Bode diagrams of $F(s)$ and $G_1(s)$ are presented in Fig. 15. In Fig. 15, the solid line represents $F(s)$, which exhibits the characteristics of notch filtering at the second and third harmonics, which compensates for the lack of bandpass filtering in $G_1(s)$ and does not cause any amplitude attenuation or phase offset at the fundamental frequency.

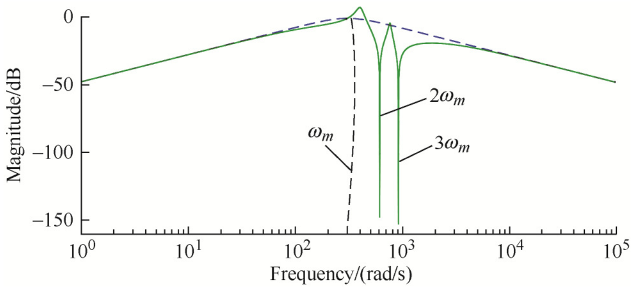

Fig. 15 Bode diagrams of $F(s)$ and $G_1(s)$

4 Simulation and experimental results

As shown in Fig. 16, the proposed DISOGI-HDN-PLL algorithm fully compensates for amplitude deviations, phase shift, DC offset, and harmonic distortion. After error compensation, the signal is sent to the PLL for decoding.

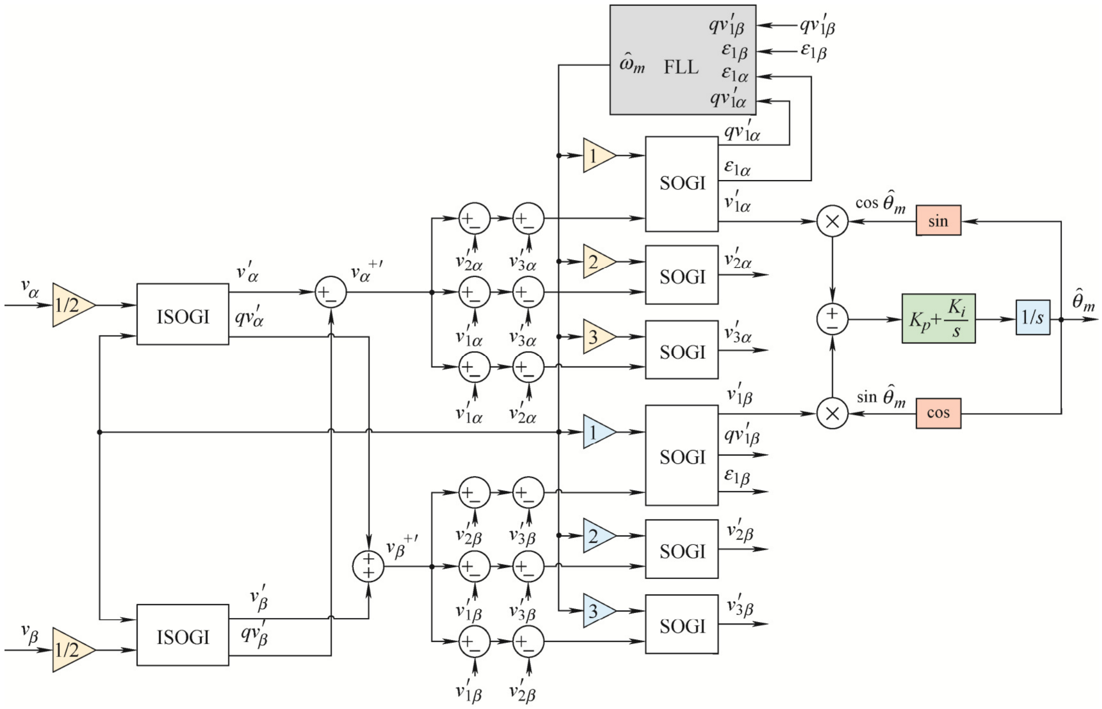

Fig. 16 Structural diagram of the DISOGI-HDN-PLL

4.1 Simulation verification

Simulink is used to verify the proposed DISOGI-HDN-PLL by setting the amplitude U_m=1 V and n=3 000 r/min. When the errors analyzed in Section 2.2 appear separately, the observed compensation effect is as shown in Figs. 17-20.

When the amplitude of one phase is α = 0.8, the comparison error between the DSOGI-PLL and the DISOGI-HDN-PLL and the reference angle is as shown in Fig. 17. When the phase shift is φ=π/18, the comparison error is shown in Fig. 18. It can be seen that the deviation range is very small, and the difference is not significant, meeting the high-precision requirements. The proposed decoding algorithm has the same amplitude error and phase error suppression ability as the DSOGI-PLL, but the proposed DISOGI-HDN-PLL has a higher response speed.

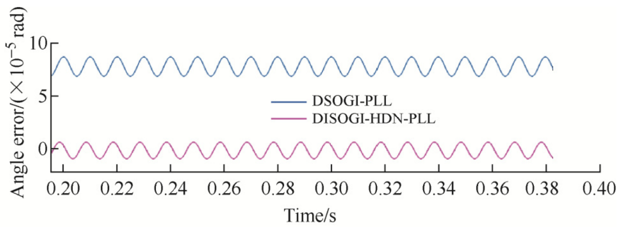

Fig. 17 Error compensation results when only amplitude deviation is present

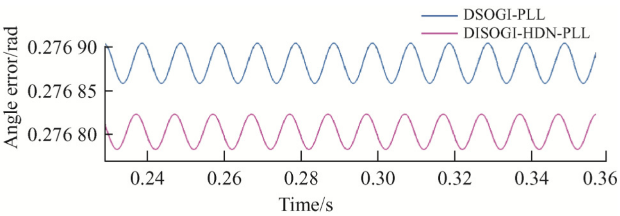

Fig. 18 Error compensation results when only phase shift is present

As shown in Fig. 19, given a sinusoidal signal with a DC offset U_{dc}=0.2 V, when reaching a steady state, the DSOGI-PLL decoding algorithm cannot eliminate the DC offset component of the input signal, so the calculated position angle cannot track the actual angle. The amplitude of the steady-state tracking error is approximately 0.151 rad. The angle-tracking error of the proposed DISOGI-HDN-PLL was 0, which verified the effectiveness of the decoding algorithm in suppressing the DC offset.

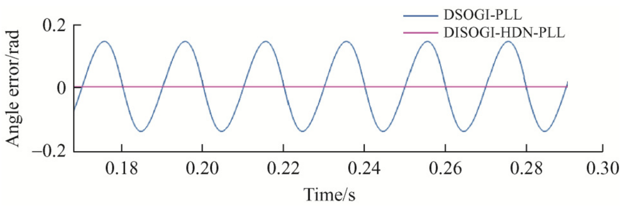

Fig. 19 Error compensation results when only the DC is offset

As shown in Fig. 20, a calculation error exists only in the presence of harmonic errors. When there are second, third, fourth, fifth, and sixth harmonics with a harmonic amplitude of 0.1 V, it can be seen that the error tracking range of SOGI-PLL is between –0.05 rad to 0.1 rad, while the proposed DISOGI-HDN-PLL has almost no suppression ability for low-order harmonics, which verified the effectiveness of the proposed algorithm in suppressing low-order harmonics.

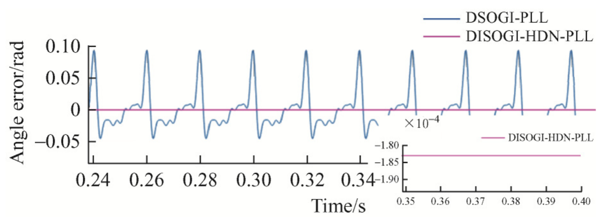

Fig. 20 Error compensation results when only harmonics are present

To verify the overall performance of the proposed algorithm, we set the amplitude U_m=1 V and n=3 000 r/min and 5 000 r/min. The test conditions included an amplitude deviation α=0.8, phase shift φ=π/18 rad, DC offset U_{dc}=0.2 V, and second and third harmonic distortions with amplitudes equal to 10% of the fundamental frequency in the output of the magnetic encoder. The angle errors at these speeds are shown in Fig. 21.

When n=3 000 r/min, the angle error is approximately 4.183 2×10^{-3} rad (14.38 angular minutes). When n=5 000 r/min, the angle error is approximately 0.018 5 rad (63.83 angular minutes), indicating that the proposed algorithm maintains high decoding accuracy even at high speeds.

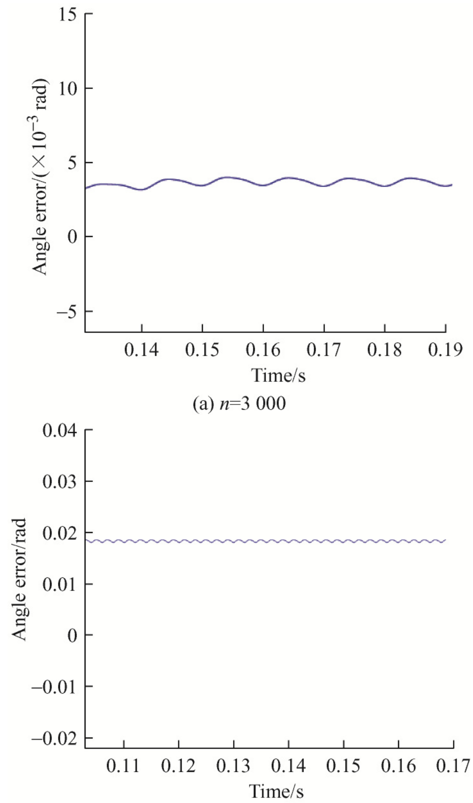

(a) n=3 000

(b) n=5 000

Fig. 21 Error between calculated angle and real angle with non-ideal error

Next, we verified the decoding performance during acceleration. The results of increasing the motor speed from 600 r/min to 3 000 r/min between 0.4 s to 1.2 s are presented in Fig. 22a. Owing to the effective suppression of the signal errors by the DISOGI-HDN-PLL, the calculated frequency before acceleration can track the real frequency with a frequency error of 0. During the 0.2 s acceleration, the calculated frequency quickly converges to the real frequency. Finally, in the steady state, the frequency error again approaches 0, indicating high accuracy.

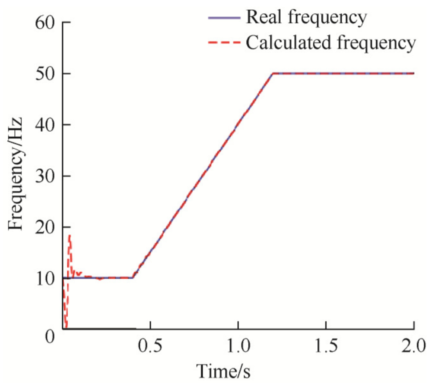

(a) Calculated and real frequencies

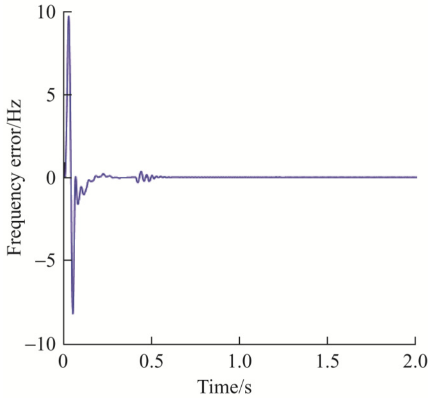

(b) Frequency errors

Fig. 22 Simulation results under acceleration

4.2 Experimental verification

The experimental setup is shown in Fig. 23, and Tab. 1 lists the main specifications of the experimental equipment. A high-precision encoder was used as the reference for motor rotor calibration and algorithm validation. The experiment included a comparative analysis of the DSOGI-PLL and the proposed DISOGI-HDN-PLL algorithms. Two scenarios were evaluated: constant velocity and constant acceleration.

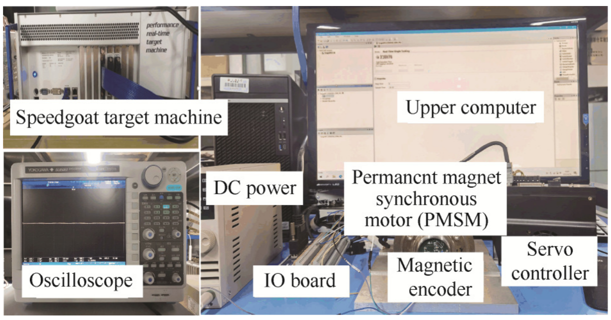

Fig. 23 Experimental platform

Tab.1 Main specifications of the experimental equipment

Device	Parameter
PMSM	5 000 r/min, 200 W
Servo controller	2.7 A, 400 W
Reference encoder	17-bit
Speedgoat-IO334-21	16 channel analog, 5MSPS
Infineon giant magnetoresistance sensor TLE5009	3.3 V, 1 MHz
Yokogawa oscilloscope DL850EV	8 channels, 100 MS/s

4.2.1 Constant speed

To measure the rotor position angle, the control system applied different speed commands to ensure that the motor operated at a constant speed. When the motor was running at 600 r/min, the ability of the proposed DISOGI-HDN-PLL to suppress harmonics and DC offset was evaluated. The fast Fourier transform (FFT) analysis of the sine and cosine signals directly outputted by the magnetic encoder and the FFT analysis after compensation using the proposed DISOGI-HDN-PLL are shown in Figs. 24 and 25, respectively.

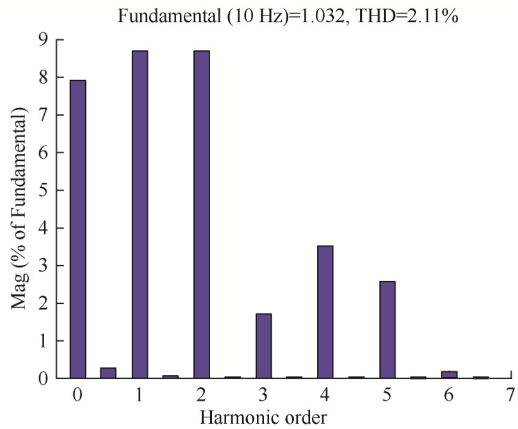

(a) FFT of sine function before compensation

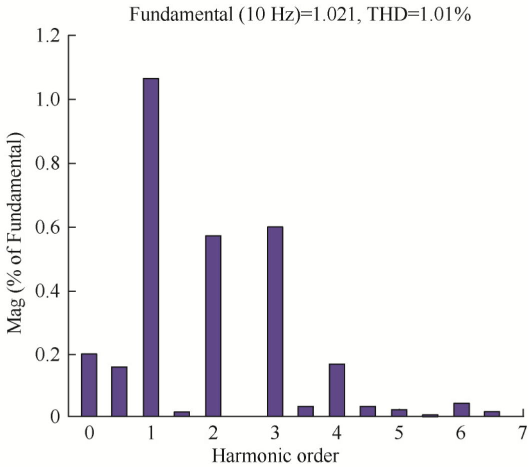

(b) FFT of sine function after compensation

Fig. 24 FFT analysis of the sine signal

Before and after compensation using the proposed DISOGI-HDN-PLL, the DC offsets of the sine and cosine components decreased from 7.96% and 2.32% to 0.19% and 0.17%, respectively. The second and third harmonic contents of the sine component decreased from 1% and 1.72% to 0.56% and 0.59%, respectively, while those of the cosine components decreased from 1.51% and 2.54% to 0.80% and 0.89%, respectively. It is noteworthy that the total harmonic distortion of the sine and cosine decreased from 2.11% and 3.10% to 1.01% and 1.23%, respectively. In addition, Fig. 24a and Fig. 25a show that the amplitudes of the sine and cosine signals were 1.032 V and 0.982 5 V before compensation, respectively, which are not equal, with an amplitude error of 0.049 5 V. After error compensation, the amplitudes of the sine and cosine signals became 1.021 V and 1.02 V, respectively, with an amplitude error of only 0.001 V. Thus, the amplitude error was effectively corrected.

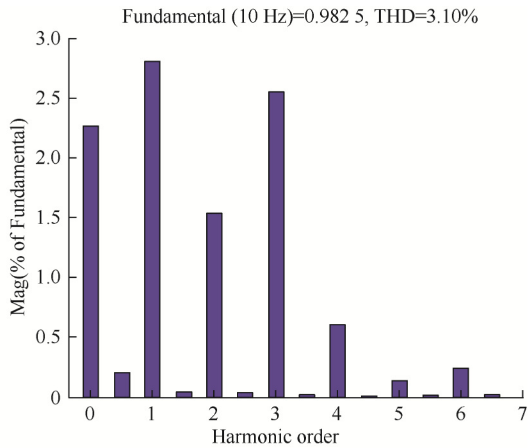

(a) FFT of sine function before compensation

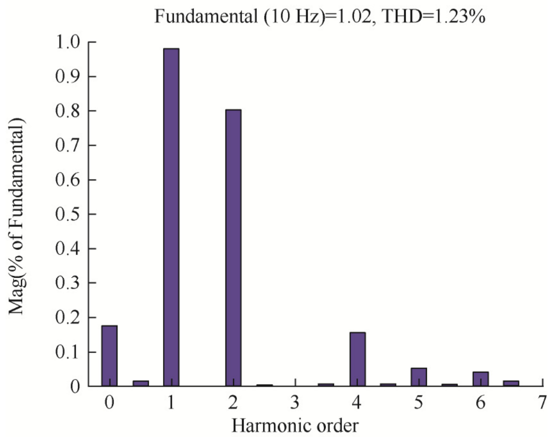

(b) FFT of sine function after compensation

Fig. 25 FFT analysis of the cosine signal

In Fig. 26, compared to the reference encoder, the angle error decreases from a range of –2.2° to 2° to a reduced range of –0.7° to 0.4° after compensation using the proposed DISOGI-HND-PLL. The results of increasing the motor speed to 2 400 r/min are presented in Fig. 27. Compared to 600 r/min, the error increases slightly, but its magnitude remains on the same order and exhibits periodic characteristics.

To verify the decoding performance of the proposed DISOGI-HDN-PLL at high speeds, the motor speed was further increased to 5 000 r/min, and the results are presented in Fig. 28. Compared to 600 r/min and 2 400 r/min, the error signal exhibits pronounced jitter, especially in the DSOGI-PLL. Nonetheless, the angle error decreases from a range of –2.3° to 2.6° to a range of –0.9° to 0.8° after compensation using the DISOGI-HND-PLL, which verifies that the decoding algorithm can still meet the high-precision requirements at high speeds.

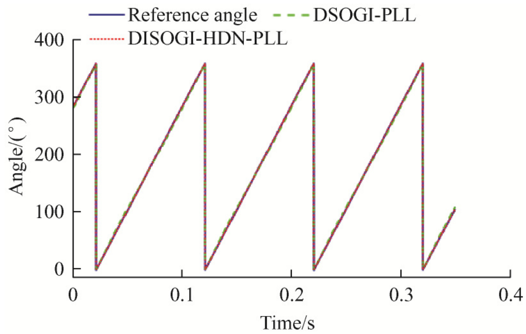

(a) Angle

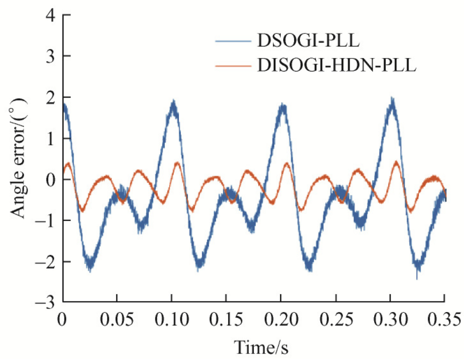

(b) Angle errors

Fig. 26 Experimental results at constant velocity n = 600 r/min between DSOGI-PLL and DISOGI-HDN-PLL

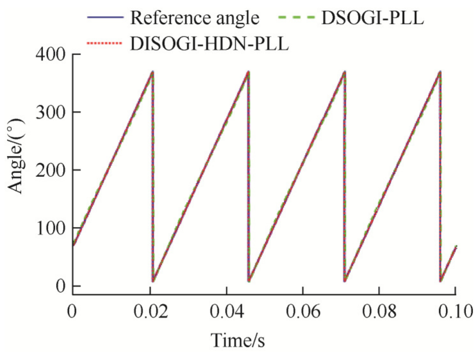

(a) Angle

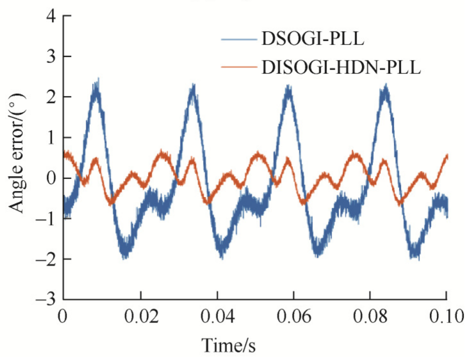

(b) Angle errors

Fig. 27 Experimental results of DSOGI-PLL and DISOGI-HDN-PLL at a constant velocity n = 2 400 r/min

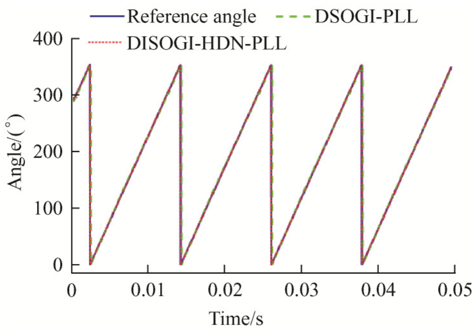

(a) Angle

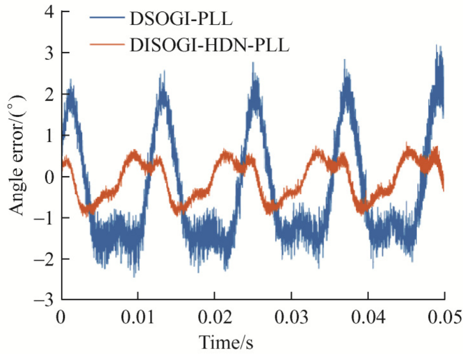

(b) Angle errors

Fig. 28 Experimental results of DSOGI-PLL and DISOGI-HDN-PLL at a constant velocity n = 5 000 r/min

4.2.2 Constant acceleration

Given the control system, different speed commands were used to operate the motor at variable speeds. The rotating speed was increased from 600 r/min to 1 200 r/min, and the corresponding signal frequency was increased from 10 Hz to 20 Hz.

From Fig. 29a and Fig. 30a, it can be seen that because of non-ideal factors, the signal frequency of the DSOGI-PLL cannot track the reference frequency accurately, resulting in a large frequency error. After acceleration, the error stabilizes within the range of –0.5 Hz to 0.5 Hz.

As shown in Fig. 29b and Fig. 30b, before acceleration, the proposed DISOGI-HDN-PLL effectively suppresses the non-ideal factors of the magnetic encoder, with the frequency error maintained between –0.03 Hz to 0.03 Hz. During the acceleration phase, as the designed second-order FLL continues to perform well, no significant increase in frequency tracking error is observed, and the frequency error remains within –0.05 Hz to 0.05 Hz, demonstrating a significant improvement in frequency tracking accuracy.

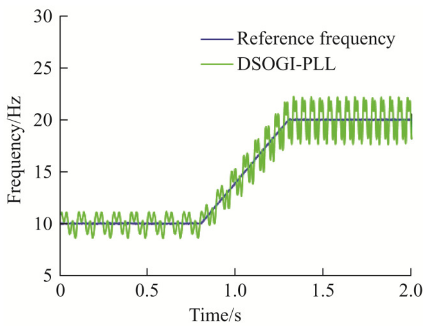

(a) DSOGI-PLL

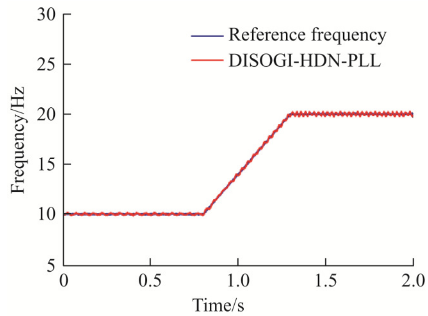

(b) Proposed DISOGI-HDN-PLL

Fig. 29 Experimental curves of actual angular frequency and estimated angular frequency during acceleration

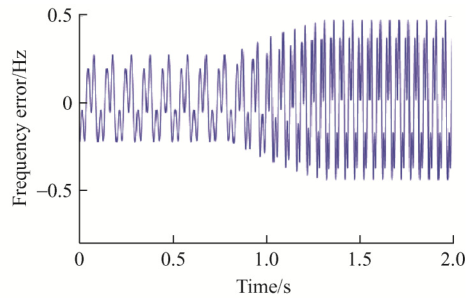

(a) DSOGI-PLL

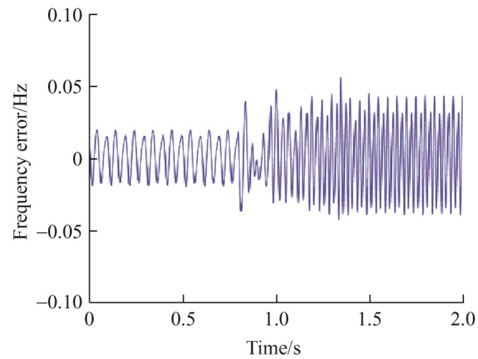

(b) Proposed DISOGI-HDN-PLL

Fig. 30 Experimental curves of frequency error during acceleration

5 Conclusions

In this study, an effective method, DISOGI-HDN-PLL, was proposed to improve the accuracy of magnetic encoder outputs. This algorithm is based on the PLL and DSOGI frameworks. The main results of this study are as follows.

(1) Compensation of the DC offset in the magnetic encoder output using DISOGI, which also compensates

for amplitude and phase errors due to the characteristics of DSOGI.

(2) To address low-order harmonics, an HDN was designed, with each phase of the HDN containing three SOGIs for extracting these harmonics. The estimated system frequency was fed back to each SOGI in real time using a designed second-order FLL, enabling closed-loop control and improving the robustness of the algorithm.

Simulation and experimental results demonstrated that at both constant speed and constant acceleration conditions, the proposed DISOGI-HND-PLL effectively corrects the sine and cosine signals output by the sensor at low and high speeds, while maintaining high angle resolution accuracy.

References

[1] G Ye, H Liu, Y Wang, et al. Ratiometric-linearization-based high-precision electronic interpolator for sinusoidal optical encoders. *IEEE Transactions on Industrial Electronics*, 2018, 65(10): 8224-8231.

[2] J Silva, D M Caetano, T Rabuske, et al. Integrated circuit for magnetic encoder sensing in TMR-based industrial positioning system. *IEEE Transactions on Industrial Electronics*, 2024, 71(8): 9904-9913.

[3] A N Montanari, E de S Oliveira. A novel analog multisensor design based on fuzzy logic: A magnetic encoder application. *IEEE Sensors Journal*, 2017, 17(21): 7096-7104.

[4] B Lequesne, T Schroeder. High-accuracy magnetic position encoder concept. *IEEE Transactions on Industry Applications*, 1999, 35(3): 568-576.

[5] M Tian, J Gu, Y Yu. Resolver-to-digital conversion based on enhanced single degree-of-freedom ADRC for acceleration position error suppression in PMSM drives. *IEEE Transactions on Transportation Electrification*, 2024, 11(10): 1-10.

[6] J W Park, H X Nguyen, T N C Tran, et al. A linear compensation method for improving the accuracy of an absolute multipolar magnetic encoder. *IEEE Access*, 2021, 9: 19127-19138.

[7] W Mi, J Yu, F Zhao, et al. Complex-vector flux-linkage envelope demodulation for high-speed resolver-to-digital conversion system. *IEEE Transactions on Industrial Electronics*, 2025, 11(10): 1-12.

[8] Y Shi, H Zhang, X Jiang, et al. Design of output voltage waveform on magnetic encoder. *Journal of Magnetism and Magnetic Materials*, 2004, 282(1): 317-320.

[9] S Yu, W Liu, X Yang, et al. Quadrature sinusoidal signals correction of magnetic encoders via radial basis function neural network and adaptive loop shaping. *IEEE Transactions on Industrial Electronics*, 2023, 70(11): 11527-11534.

[10] T N C Tran, H X Nguyen, J W Park, et al. Improving the accuracy of an absolute magnetic encoder by using harmonic rejection and a dual-phase-locked loop. *IEEE Transactions on Industrial Electronics*, 2019, 66(7): 5476-5486.

[11] Q Lin, T Li, Z Zhou. Error analysis and compensation of the orthogonal magnetic encoder. *2011 First International Conference on Instrumentation*, *Measurement*, *Computer*, *Communication and Control*, October 21-23, 2011, Beijing, China. IEEE, 2011: 11-14.

[12] Y Wang, X Bao, W Hua, et al. Implementation of embedded magnetic encoder for rotor position detection based on arbitrary phase-shift phase-lock loop. *IEEE Transactions on Industrial Electronics*, 2022, 69(2): 2033-2043.

[13] H C Chuang, C W Kung, L W Chen, et al. Nonlinear error correction for magnetic encoders. *IEEE Sensors Journal*, 2023, 23(9): 9129-9135.

[14] S Wang, Z Li, L He, et al. Demodulation algorithm of magnetic encoder with specified harmonic elimination. *IEEE Transactions on Instrumentation and Measurement*, 2024, 73(1): 1-9.

[15] S Wang, J Li, J Zhao, et al. High response decoding system of resolver considering signal errors. *IEEE Sensors Journal*, 2023, 23(16): 18682-18691.

[16] Đ Stojić, S Veinović, L Ivanović. Improved stator flux estimation in sensorless AC motor drives using extented SOGI. *2023 22nd International Symposium on Power Electronics (Ee)*, December 3-5, 2023, Novi Sad, Serbia. IEEE, 2023: 1-5.

[17] F Xiao, L Dong, L Li, et al. A frequency-fixed SOGI-based PLL for single-phase grid-connected converters. *IEEE Transactions on Power Electronics*, 2017, 32(3): 1713-1719.

[18] Z Xing, L Guo, L Wang, et al. A DSOGI phase lock loop

method based on internal model for grid voltage. *Journal of Electrical Engineering*, 2018, 13(7): 1-7.

[19] J Bergas-Jané, C Ferrater-Simón, G Gross, et al. High-accuracy all-digital resolver-to-digital conversion. *IEEE Transactions on Industrial Electronics*, 2011, 59(1): 326-333.

[20] H Cho, E K Kim, E Jang, et al. Improved positioning method for magnetic encoder type AGV using extended Kalman filter and encoder compensation method. *International Journal of Control*, *Automation and Systems*, 2017, 15(1): 1844-1856.

[21] H V Hoang, J W Jeon. Signal compensation and extraction of high-resolution position for sinusoidal magnetic encoders. *2007 International Conference on Control*, *Automation and Systems*, October 17-20, 2007, Seoul, Republic of Korea. IEEE, 2007: 1368-1373.

[22] Y Wang, H Ahmed, H Zhang, et al. Feedforward PLLS for motor position estimation using embedded magnetic encoder. *IEEE Sensors Journal*, 2024, 24(7): 10307-10315.

[23] T N C Tran, H X Nguyen, J W Park, et al. Improvement of the accuracy of absolute magnetic encoders based on automatic calibration and the fuzzy phase-locked-loop. *IECON 2017 - 43rd Annual Conference of the IEEE Industrial Electronics Society*, October 29-31, 2017, Beijing, China. IEEE, 2017: 3310-3315.

[24] K K Tan, K Z Tang. Adaptive online correction and interpolation of quadrature encoder signals using radial basis functions. *IEEE Transactions on Control Systems Technology*, 2005, 13(3): 370-377.

[25] K Tan, H Zhou, T H Lee. New interpolation method for quadrature encoder signals. *IEEE Transactions on Instrumentation and Measurement*, 2002, 51(5): 1073-1079.

[26] X Song, J Fang, B Han, et al. Adaptive compensation method for high-speed surface PMSM sensorless drives of EMF-based position estimation error. *IEEE Transactions on Power Electronics*, 2016, 31(2): 1438-1449.

[27] J Kang, B Hao, Y Su, et al. Improving the accuracy of multipole magnetic encoder by three-phase hall. *IEEE Sensors Journal*, 2023, 23(13): 13987-14001.

[28] L Wang, X Wei, Z Li, et al. Research on suppression method of jump points for multipole magnetic encoder based on fuzzy logic and ant colony optimization. *IEEE Sensors Journal*, 2023, 23(23): 28733-28743.

[29] S Hao, Y Liu, M Hao. Study on a novel absolute magnetic encoder. *2008 IEEE International Conference on Robotics and Biomimetics*, February 22-25, 2009, Bangkok, Thailand. IEEE, 2009: 1773-1776.

[30] W Mi, Q Li, F Jian, et al. A novel all-digital resolver-to digital conversion system based on numerical synchronous integration. *IEEE Transactions on Industrial Electronics*, 2023, 70(9): 9623-9631.

[31] P Liu, Z Wu. Anti-harmonic phase detector for PLL in resolver-to-digital conversion. *IEEE Transactions on Industrial Electronics*, 2025, 72(4): 4291-4300.

[32] L Guo, Q Ye, N Jin, et al. Sliding-mode observer-based grid voltage-observation method with frequency-fixed dual SOGI and cross-compensated phase-locked loop. *Chinese Journal of Electrical Engineering*, 2024, 10(3): 37-49.

[33] A Zambrano, H G Kerkhoff. Improving the dependability of AMR sensors used in automotive applications. *2017 22nd IEEE European Test Symposium (ETS)*, May 22-26, 2017, Limassol, Cyprus. IEEE, 2017: 1-2.

[34] A Arami, J D Rechenmann, K Aminian. Reference-free auto mated magnetic sensor calibration for angle estimation in smart knee prostheses. *IEEE Sensors Journal*, 2014, 14(6): 1788-1796.

Shuang Wang (Member, IEEE) received the B.S., M.S., and Ph.D. degrees in Electrical Engineering from the Harbin Institute of Technology, Harbin, China, in 2000, 2005, and 2009, respectively.

He is currently an Associate Professor with the School of Mechatronic Engineering and Automation, Shanghai University, Shanghai, China. His research interests include power electronics, sensors, and motor drives.

Hanyi He was born in Anhui, China in 2002. He received the B.S. degree in Electrical Engineering from Shanghai Maritime University, Shanghai, China, in 2022. He is currently pursuing the M.S. degree at the School of Mechatronic Engineering and Automation, Shanghai University, Shanghai, China.

His research interests include motor drive and resolver decoding.

Tianren Li received the B.S. degree in Electrical Engineering from Shanghai University, Shanghai, China, in 2023. He is currently pursuing the M.S. degree at the School of Mechatronic Engineering and Automation, Shanghai University, Shanghai, China. His research interests include resolver decoding.

Hao Li received the B.S. degree in Electrical Engineering and Automation from the School of Mechatronic Engineering and Automation, Shanghai University, Shanghai, China, in 2024. He is currently pursuing the M.S. degree at the School of Mechatronic Engineering and Automation, Shanghai University, Shanghai, China.

His research interests include motor drives, magnetic encoder decoding and signal processing.

Jianfei Zhao received the B.S. and M.S. degrees in Mechatronic Engineering from Xi'an Jiaotong University, Xi'an, China, in 2000 and 2003, respectively, and the Ph.D. degree in Electrical Engineering from Shanghai Jiao Tong University, Shanghai, China, in 2012.

From 2003 to 2006, he worked as a Research and Development Engineer and Project Manager at the Research and Development Center, Myway-labs Company, Yokohama, Japan. He is now an Associate Professor with the School of Mechatronic Engineering and Automation, Shanghai University, Shanghai. His research interests include power electronics and electronic vehicles.